3D printable fully biomass-based composite using poly(furfuryl alcohol) as binder and cellulose as a filler

K. Bouzidi, D. Chaussy, A. Gandini, R. Bongiovanni, D. Beneventi

To cite this version:

K. Bouzidi, D. Chaussy, A. Gandini, R. Bongiovanni, D. Beneventi. 3D printable fully biomass-based composite using poly(furfuryl alcohol) as binder and cellulose as a filler. Carbohydrate Polymers, 2022, 293, pp.119716. 10.1016/j.carbpol.2022.119716 . hal-03747901

HAL Id: hal-03747901
https://hal.science/hal-03747901v1

Submitted on 9 Aug 2022

3D printable fully biomass-based composite using poly(furfuryl alcohol) as binder and cellulose as a filler

K. Bouzidi, [a,*] D. Chaussy,[a] A. Gandini, R. Bongiovanni [b], D. Beneventi [a]

[a] Univ. Grenoble Alpes, CNRS, Grenoble INP[+], LGP2, 38000 Grenoble, France

[+] Institute of engineering Univ. Grenoble Alpes

[b] Department of Applied Science and Technology, Politecnico di Torino, Torino, 10129 Italy

* Corresponding author

Email address: Khaoula.bouzidi@grenoble-inp.fr

Abstract

Nowadays, composite materials are widely used in different sectors owing to their improved mechanical and functional properties compared to bulk materials and efficient manufacturing processes. Nevertheless, the majority of these materials are still petroleum-based, which is incompatible with the recent environmental awareness. As a result, in the current study, a fully biomass-based composite material was produced employing poly(furfuryl alcohol) (PFA) as a bio-based matrix coupled with cellulose powder as fillers and processing aid agent. The addition of cellulose powder increased the viscosity of the uncured composite paste and conferred it a shear-thinning thixotropic making it suitable for 3D printing using the liquid deposition modeling technique (LDM). After curing, the combination of these raw materials yields a renewable and cost-effective composite for additive manufacturing by the LDM technique with high interlayer and interfilament adhesion, good mechanical performances and adequate shape fidelity.

Keywords: Cellulose, Poly(furfuryl alcohol), Additive manufacturing, rheology, biocomposite

1 Introduction

Recently, Additive Manufacturing (AM) is getting more and more popular in many fields and for many applications that require different materials. In AM by material extrusion one can notice the dominance of thermoplastics which are for the most part petroleum-based. Under the upraising environmental concerns, many research works have been conducted to find a substitute for the use of thermoplastics and among the suggested materials one can notice cellulose and, more generally, polysaccharides and lignocellulosic materials. The latter bio-based material is particularly interesting for 3D printing as it is available, renewable, cost-effective, and lightweight. However, these advantages come with a major limitation: cellulose cannot be melted hence is not compatible with AM by melt extrusion. Therefore, researchers suggested several formulations using different forms of cellulose for printing by cold extrusion in particular hydrogels of nano and micro fibrillated cellulose and cellulose nanocrystals which were compatible with this AM technique (Abouzeid et al. 2018; Håkansson et al. 2016; Leppiniemi et al. 2017; Markstedt et al. 2015; Sultan et al. 2017). Nonetheless, the use of these cellulose-based hydrogels, and in some cases suspensions and solutions (Pattinson et Hart 2017), raised additional challenges and limitations to its printability such as an important shrinkage upon drying due to a limited solid content in the formulation (Klar et al. 2019; Thibaut et al. 2019) or a complicated and expensive freeze-drying process (Jiang, Oguzlu, et Jiang 2021; Markstedt et al. 2015).

On the other hand and from a more technical point of view, thermoplastics have limited thermal stability making the use of the 3D printed parts limited to low-temperature environments (Krajangsawasdi et al. 2021; Vinyas et al. 2019). Despite the existence of technical thermally stable printable filaments such as PolyEther Ether Ketone (PEEK) and PolyEthylenImine (PEI), they are still expensive (up to 790 $/kg) and rather complicated to print (Berretta et al. 2017; Han et al. 2019; Niu et al. 2021). To overcome these thermal performances limitation when using thermoplastics, several articles have been published about formulations compatible with AM by extrusion of composites with the use of thermosetting resin with better thermal and mechanical performances (Compton 2015; Compton et al. 2018; Hmeidat et al. 2020; Hmeidat, Kemp, et Compton 2018; Lei et al. 2019; Malek et al. 2017; Shang et al. 2017; Shi et al. 2017; Yang et al. 2017). Nonetheless, the majority of the suggested composites are still fossil-based. To overcome these limitations the intention of the present work is to develop a 3D printable material by AM by Liquid Deposition Modeling (LDM) using cellulose fibers as bio-based and cost-effective filler along with a bio-based thermosetting resin which will play the role of a binder. This mixture would yield a fully bio-based printable composite with a lower environmental impact compared to the fossil-based thermosetting resins and more particularly the much-used epoxy resin with 5 times less impact of the polymer production on climate change (Hong, Zhou, et Hong 2015;

La Rosa et al. 2013). However, an optimization step should be done to define the appropriate proportions to obtain a printable ‘ink’ and optimal performance of the cured printed biocomposite.

In no uncertain terms, LDM is inseparable from rheology. One cannot begin LDM without first questioning the rheological properties of the formulation. Indeed, these properties determine the range of structures that can be printed, the optimal printing parameters, and ultimately the quality of the printed part. Despite this, the manner in which rheology ties in with these considerations has to date not been specified well in the literature. Some work has been done to identify some of the important rheological requirements of the ink formulation and suggested a range of values these properties should take for a successful print (Feilden 2017).

However, up to this point, the term ‘printability’ or ‘printable’ has been used without defining exactly what is printability, and what qualifies material as printable. In a general manner, printability is a measure of how suitable a suspension’s properties are for AM by a certain technique, which in our case is cold material extrusion. As much as this printability concept can seem to be almost innate, especially for researchers that have been working on AM by material extrusion (called also direct ink writing, liquid deposition modeling, or robocasting in the literature), up to now there is not a clear and standardized method to define this emergent concept. However, in the literature, we can find few attempts to define some criteria and figures of merit.

In 2017, a figure of merit was suggested by (Feilden, 2017) which is only based on the rheological properties of the paste formulations, thus allowing a rapid selection of a promising formulation for AM by material extrusion. This figure of merit was developed based on the rheological properties required, experimental work, and the state of art, for a successful printing, such as:

- Maximizing G’ to minimize the elastic deformation during printing, hence shape maintenance.
- Minimizing the flow index n, the consistency coefficient K and the yield stress τ_y to reduce the force required to bend the extruded filament, to deposit it gently without deforming the printed layers.
- Nonetheless, τ_y should not drop from a minimum value in order to resist the surface forces and gravity.
- Minimizing the yield shear rate γ_y to reduce the paste compressibility during extrusion for an instant break of extrusion, when needed.

Accordingly, a paste-specific figure of merit (Φ) was suggested and a minimum value of 20 was found to be required for a successful robocasting (eq 1).

$$\Phi = \frac{G'}{\tau_y} \qquad \textit{eq 1}$$

In the most recent work (Duty et al. 2018), a more general viscoelastic model was proposed based on the rheological and thermophysical properties of the ink and the processing parameters. This model establishes a methodical approach to characterize printability by providing different equations serving printing criteria for a series of conditions that must be satisfied in order to successfully print a part. These equations depend not only on the material properties but also on the used hardware and time-depending printing parameters. In the literature, we also come across other attempts to define the concept of printability for AM by material extrusion, but they focus more on assessing the printing quality, with no clear definition of a figure of merit for the ink itself (Gillispie et al. 2020; Naghieh et Chen 2021).

In the present work, the figure of merit (Φ), coupled with maximization of paste stiffness G', were considered as criteria to optimize the ink formulation as this approach is paste-based without compassing printing parameters. Later, the effect of a few printing parameters on the flexural properties of the cured and printed material will be assessed.

2 Materials and methods

2.1 Materials and paste formulation

The paste formulation is prepared based on the use of a fully bio-based thermosetting furanic resin which is the poly(furfuryl alcohol) (PFA) and cellulose powder as a filler and rheology modifier. In the present work, the used furanic resin is a commercial product kindly supplied by Transfuran Chemicals along a latent catalyst enabling the crosslinking at high temperatures. The PFA resin contains less than 1% of free furfuryl alcohol monomers and 7.5% water. The viscosity is 3.8 ±0.3 Pa·s as experimentally determined. The used catalyst is an aqueous solution of (2-hydroxyethyl) ammonium nitrate.

As for the fillers, the cellulose powder is a commercial product by CFF and was kindly supplied by Rossow Industry. The mainly used cellulose is the finest powder in this product line, known under the trade name Technocel® FM8. According to the supplier's datasheet, this cellulose has a powdery aspect, with over 99.5% purity, and 80% whiteness. The high purity of the product was further confirmed with a FTIR, NMR and Xray spectrum which revealed a pure type I cellulose with over 77% crystallinity index measured using the peak height method (Segal et al. 1959). Moreover, the particle size was reported to be between 6-12 µm which was further checked with granulometry analysis revealing that 50% of the particle have a size under 9 µm. Furthermore, as is visible in the SEM image (Figure 1), these cellulose particles are rod-shaped with a limited form factor. The specific density of cellulose powder is 1.5 g/cm^3.

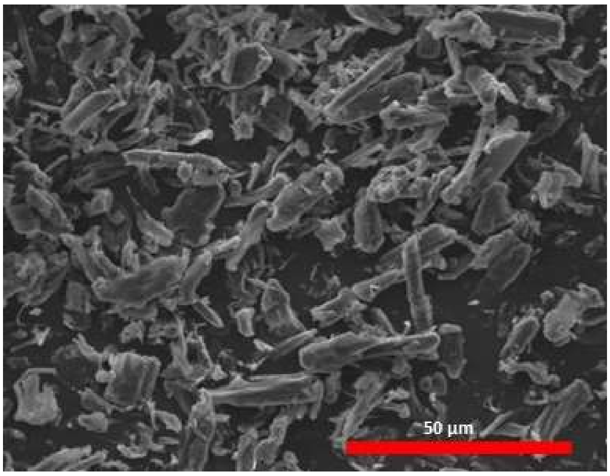

Figure 1: SEM image of the used cellulose powder

The slurries or 'pastes' were prepared by first adding the catalyst to the resin and manually mixing the two fluids. The mixture was then poured into a planetary mixer (KitchenAid 5KSM3311X) at room temperature and the cellulose powder was gradually added for 5 min while mixing at 120 rpm. The slurry was further blended for 15 minutes at 180 rpm and then 5 min at 200 rpm. The resulted paste is then manually loaded in syringes with precaution to avoid creating any air bubbles and voids. These cartridges are sealed and then placed in a refrigerator at 4-5°C before further processing to prevent any crosslinking of the polymer during the storage.

In this study, different formulations were tested with different cellulose fractions and water content. As a first step, preliminary formulations were tested using different fiber morphology, different solvent content, and different resin/cellulose ratios. In the light of these preliminary tests we noticed that the total solvent content in the formulation should not exceed 20% (32% of the polymeric matrix) to avoid any cracking and defect in the composite upon crosslinking. On the other hand, the cellulose weight fraction cannot exceed a maximum of 30%, which leads to a powdery crumbly aspect of the mixture. Moreover, it was found that less than 10 wt% of cellulose powder yields a diluted suspension with a law bulk yield stress which is needed in the formulation so that the ink maintains the shape of the die after extrusion, which is very important for 3D printing. Finally, the use of fine cellulose particles is privileged to avoid any extrusion defects and to make possible the use of small nozzles without clogging. These conclusions leave us with a better-targeted formulation composition. For further optimization of the paste, 6 formulations were prepared with cellulose weight fractions ranging from 16 to 29 wt% and with no extra added solvent to the PFA oligomers. The formulations presented in this work contain 16, 19, 22, 25, 28, and 29 wt% of cellulose powder referred to using the following code PFA-CellX-B where X is the cellulose content in the formulation.

2.2 3D printing by cold material extrusion

The main used machine for additive manufacturing is a commercial 3D printer Artillery sidewinder (China). The printing platform moves on the Y-axis whereas the printing head moves in x and z axes. This printer is designed for fused filament printing and was upgraded with an LDM extruder. The paste formulation is fed to the extruder using a pressure syringe and then the paste is driven by the Archimedes screw to be later extruded through a nozzle with a diameter ranging from 0.5 to 2 mm. The used slicer was Simplify 3D with which is possible to program several printing parameters, such as; (i) the layer height which is the thickness of the layer deposited by the nozzle tip, (ii) the road/raster width which is the width of the material bead used for rasters, and (iii) raster angle which refers to the angle of the raster pattern with respect to the X-axis on the bottom part layer. These parameters are illustrated in Figure 2.

Besides developing and optimizing the rheology and the printability of the paste and calibrating the extrusion flow for a continuous and homogeneous flow, the printing parameters have a major effect on the printing quality and the final material's mechanical performances. Therefore, the effect of road parameters and layer height on mechanical performance was studied.

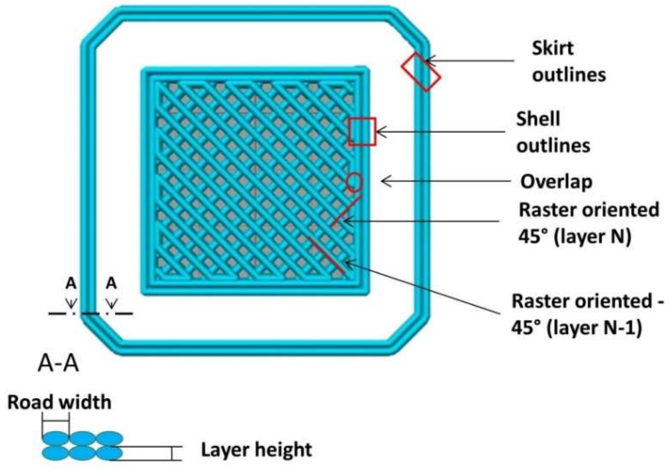

Figure 2: Simulation of printed cube done with Simplify3D with a highlight of different printing parameters.

2.3 Characterizations

Rheology

To assess the rheological behavior of the pastes and the resin, a parallel plate of 25 mm in diameter was used on an MCR 301 rheometer (Anton Paar, Austria). The gap between the plate and the platform was set to 1 mm and the temperature was fixed at 25°C. Before any rheological measurements, the fluids were sheared at a shear rate of 100 1/s for 200 seconds, followed by a rest of 200 seconds to remove any previous shear history. The samples were covered during the tests to avoid any solvent evaporation.

To perform the flow curve experiments, the shear rate was increased from 0.1 to 100 1/s or 1000 1/s depending on the paste nature during which the viscosity was recorded.

To assess the thixotropic behavior of the pastes, the shear rate was fixed at 100 1/s for 60 s before a sudden drop to 0.1 1/s. The rheological behavior in terms of viscosity trends as well as stress response was evaluated as a function of time.

Oscillatory tests were also conducted to evaluate the viscoelastic properties of the prepared pastes. To do so, amplitude sweep tests were performed at the frequency of 1 Hz and strain ranging from 0.001 to 100%. The evolution of the storage modulus (G’) and loss modulus (G”), as a function of strain, or stress was analyzed.

To check the reproducibility of the rheological measurements, especially when using concentrated slurry the tests were duplicated at least 3 times.

Morphology

The morphology of the composite surface and cross-section were investigated by scanning electron microscopy (SEM). The specimens were gold coated and examined using a QuantaFEG250 instrument. The accelerating voltage was fixed at 2.50 kV and the magnitude between 60 and 2000. The shape fidelity of 3D printed objects was evaluated by comparing the 3D digital model to 3D scans of 3D printed and cured samples. 3D scans were recorded using an in house developed scanner composed by a laser profiler (Keyence, LJ-V7080) mounted on a 6 axis robot (Staubli, TX2 60). Scans were performed with a lateral definition of 50 µm and scan speed and sampling frequency of 50 mm/s and 1 kHz, respectively, in order to obtain base square (50x50 µm) pixels. Scans were processed using the Keyence LJ-X Observer software to extract relevant sample dimensions

Mechanical characterization

The printed specimens are cured at 90°C overnight followed by a step of post-curing for 3 hours at 130°C. Before any mechanical testing, the composites were conditioned at 23°C and 50% relative humidity for at least 16 h. The mechanical properties were tested with an Instron Universal testing machine (Instron, USA), and the data were analyzed with the help of the Blue Hill software. The flexural properties were measured according to ISO 178 at a crosshead speed of 2 mm/min and 64 mm support span and using specimens with dimensions of 10 mm x 40 mm x 80 mm. The obtained data were the average of 10 to 15 measurements.

3 Results and discussion

3.1 Formulation optimization

The ‘ink’ formulation is a very important step towards successful additive manufacturing by material extrusion. A simple suspension containing cellulose particles as the solid phase and PFA oligomers as the liquid phase is aimed to be prepared. The ink suspension will thus contain 3 main components, cellulose particles as fillers, PFA oligomers as the binder, and water as resin diluents. As mentioned before, preliminary tests, enable the identification of the optimization area by identifying 6 formulations that are placed on the ternary diagram in Figure 3. The formulations are considered to be printable, when are continuously extrudable through a 1 mm nozzle and able to maintain their shape after the deposition of at least 4 layers, the poorly printable formulations are those printable but with frequent nozzle clogging otherwise the formulation is considered to be not printable. In the next section, the ink formulation will be further optimized by assessing printability which is carried out through the characterization of the different formulations according to a rheological approach.

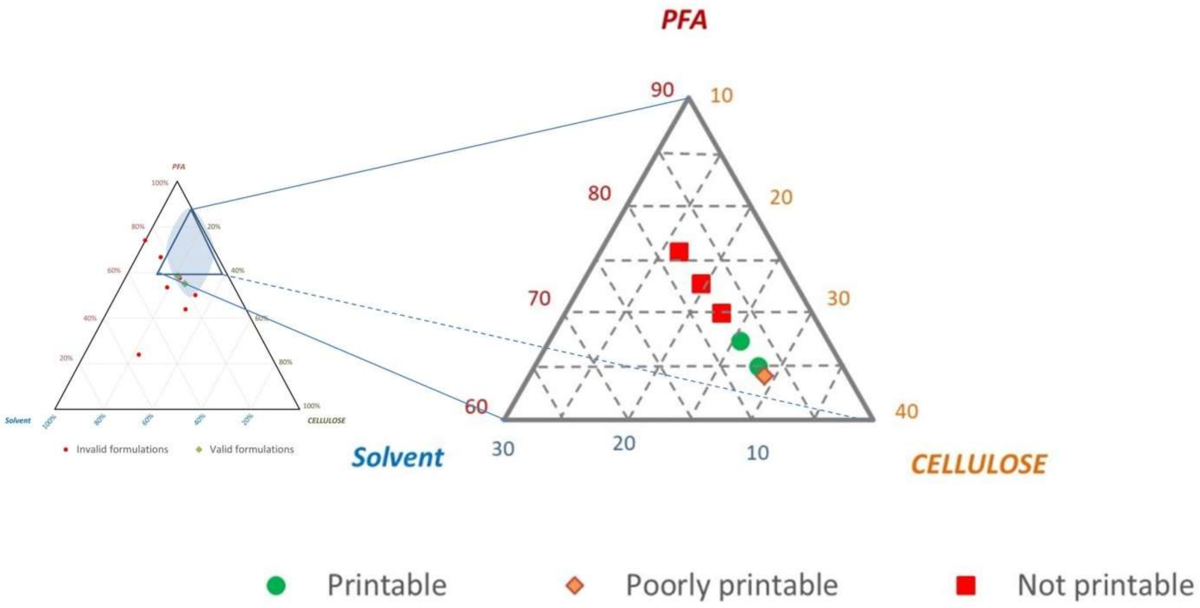

Figure 3: Ternary diagram of the different identified formulations.

Effect of cellulose concentration on the rheological behavior and the printability of the suspensions

In the absence of a clear definition of printability with material extrusion, if we rely on the different criteria leading to a successful printing in the recent literature (Beach et al. 2021; Chu, Li, et Kwan 2021; Duty et al. 2018; Fahmy, Becker, et Jekle 2020; Gillispie et al. 2020; Montoya et al. 2021; Naghieh et

Chen 2021; Panda et al. 2017; Panda, Unluer, et Tan 2018, 2019; Rieger et al. 2021; Zhang et al. 2019), we can define 3 main rheological properties:

- Shear-thinning behavior to facilitate the extrusion of the ink through different nozzles
- Optimized yield stress and stiffness of the ink formulation to ensure maximum shape fidelity and minimum structure slumping without affecting the extrudability
- Thixotropic behavior for a good viscosity recovery upon extrusion to avoid layer slump

These properties will be assessed in the next 3 subsections.

Shear-thinning behavior

To assess the slurries' flow under different shear rates, rotational rheological measurements were performed. Figure 4-A shows that the neat PFA resin (red curve) has a Newtonian flow where the viscosity is independent of the applied shear rate, whilst the addition of cellulose powder led to a shear-thinning flow. This shear-thinning behavior is more or less marked for each formulation. Thus, in order to quantify the shear-thinning degree, a fitting of the apparent viscosity versus shear rate curves with the power-law (eq 2) was done. To do so, a log-log plot of the apparent viscosity vs. shear rate was used to compute the values of n and K by linear regression over the linear portions. The values of n and K of different formulations are given in Figure 4-B. One can notice a clear interdependency between the cellulose fraction in the different suspensions and their consistency index K which increases from barely 155 Pa·s^n when adding only 16 wt% of cellulose to over 2.5 10^3 Pa·s^n with 28 wt% cellulose.

$$\mu = K\,\dot{\gamma}^{1-n} \qquad \textit{eq 2}$$

On the other hand, the thinning exponent n decreases with increasing filler fraction, dropping from 0.65 for the formulation containing 16 wt% cellulose, to 0.1-0.3 when exceeding 19 wt% of cellulose. Over a certain filler fraction, no clear correlation can be concluded between the shear-thinning ability and the content of the filler. This can be explained by the fact that by adding only 16 wt% of particle, the network is not strong enough to resist shearing forces and could easily be broken and flow, thus leading to a negligible dependence between the viscosity and the shear stress. However, when reaching a critical fraction of the fillers, the network starts to be stronger and the inter-particle interactions become dominant, thus making the structure flow more dependent on the shear stress applied. After this critical point, the shear-thinning mechanism does not change, thus making the thinning exponent insensitive to the filler content. The values of n are in agreement with those of other printable mixtures of viscoelastic materials (Feilden et al. 2016; Li, Liu, et Lin 2016; M'Barki et al. 2017; Thibaut et al. 2019).

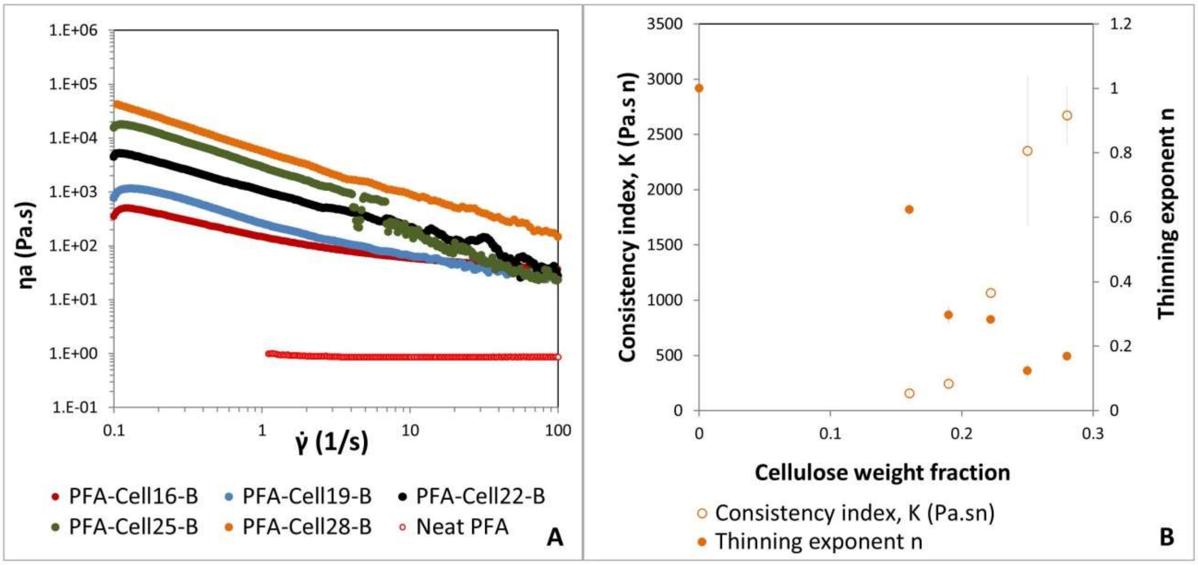

Figure 4: Rotational rheology of different slurries. (A) Flow curves and (B) values of the consistency index K and thinning exponent n.

Oscillatory rheology tests

In order to assess the viscoelastic properties of the different formulations, an amplitude sweep was performed. Figure 5 shows the storage and loss moduli (G' and G", respectively) of different slurries. As one can notice, in the Linear ViscoElastic Region (LVER), the G' value is more or less stable, which defines the stiffness of the formulation (G' LVER) which is, as discussed before, crucial to printability assessment. Then, as stress increases, the storage modulus drops until below the loss modulus. The crossover point, associated with the breakdown of the particle network within the slurry, can serve as an approximation of the yield stress τ_y. The stiffness expressed by the G' (LVER) and the yield stress values of the tested slurries are plotted in Figure 6-A. One can notice that with the addition of cellulose particles, there is an important increase of several orders of magnitude in the stiffness and yield stress.

Therefore, to select the most printable formulations, the merit figure (eq 1) suggested by (Feilden, 2017) was used. It was recommended that the value of Φ be superior to 20, based on the analysis of different printable formulations in the literature that were declared printable by material extrusion. A plot of stiffness (G' LVER) against the yield stress (τ_y) of each formulation is presented in Figure 6-B. The first criterion to classify printable and unprintable formulations is the absolute value of Φ, the line delimiting the value Φ= 20 is highlighted, but all the tested formulations were above this minimum value and the highest value is that of the formulation PFA-Cell28-B.

The second criterion is the minimum yield stress necessary to bear the gravitational forces for a certain build height. This criterion was already suggested in the literature, based on the yield stress required to withstand both forces of gravity and surface tension (M'Barki, Bocquet, et Stevenson 2017). The printability criterion (Ξ) suggested by the authors is given by eq 3, where τ_y is the paste's yield stress, ρ the density of the paste, Υ_s the surface tension, h the height of the part, *g* gravitational acceleration, and R the radius of curvature of the smallest printed feature.

$$\Xi = \frac{\tau y}{\rho g h + \gamma s \, R^{-1}} \qquad \textit{eq 3}$$

By neglecting the effect of the surface tension and considering only the effect of gravitational forces, this criterion (eq 3) can be simplified and the yield stress can be expressed in terms of the building height according to eq 4. If we consider a minimum build height of h= 10 mm the yield stress value should be above 146 Pa. The upper limit of the yield stress can be determined by the extruder force.

Respecting these criteria, the formulations with the highest printability potential are those containing over 25 wt% of cellulose (highlighted in green in Figure 6-B). Furthermore, by applying printability criteria (J. E. Smay et al. 2002), which consist of maximizing the stiffness of the suspension for better-spanning structures (eq 7), the formulations containing 28 wt% and 29 wt% are more advantaged.

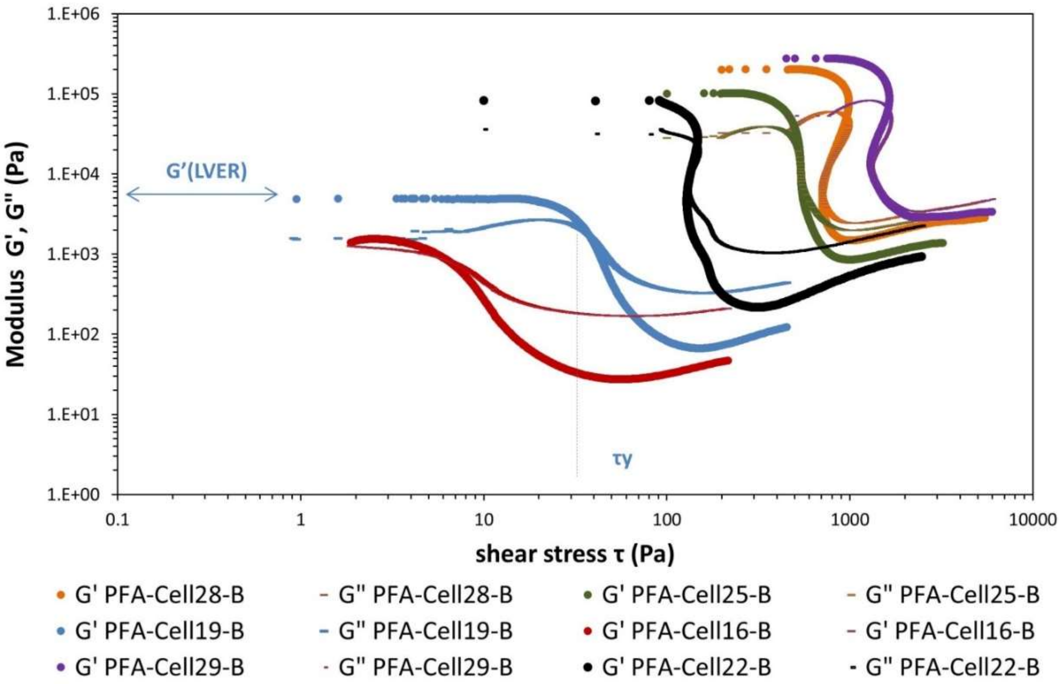

Figure 5: Storage and loss moduli vs. shear stress obtained by amplitude sweep at 1 Hz for different suspensions.

$$\tau_y = h \cdot \rho \cdot g \qquad \text{eq 4}$$

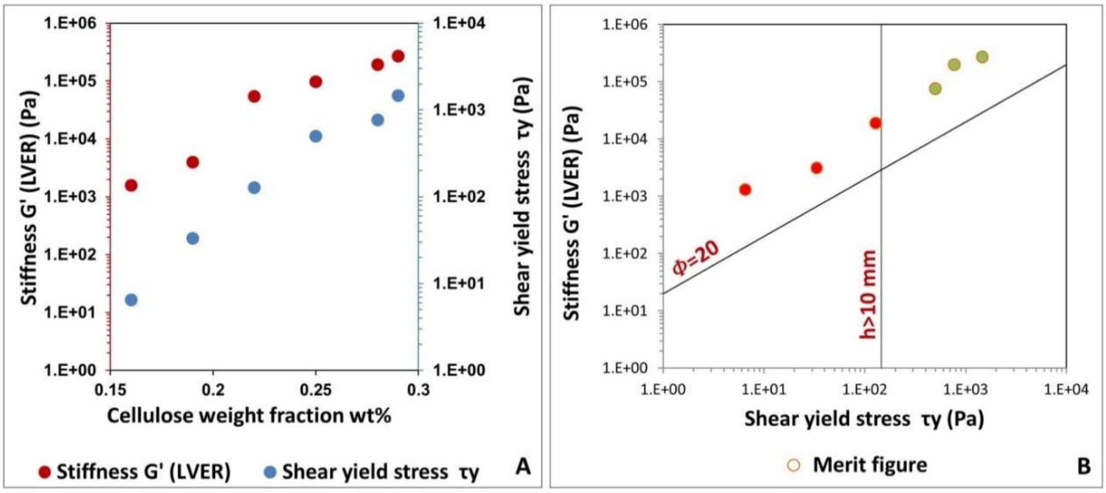

Figure 6: (A) Evolution of the yield stress and stiffness as a function of cellulose weight fraction and (B) formulation selection map showing a minimum merit figure and minimum printable object without collapsing.

Shear recovery behavior

During 3D printing with material extrusion, the inks experience shear forces and undergo physical changes, especially for complex fluids. The thixotropic rheological component of the different suspensions should be examined because it has crucial importance in the extrusion-deposition process. Indeed, ideally, the viscosity of the developed ink should decrease at high shear rates to facilitate the extrusion process (shear-thinning) and increase immediately after a total recovery at the outlet of the nozzle (Kraut et al. 2017; Lille et al. 2018). To investigate the thixotropy of formulations, a 5-step experiment was applied to model the high shear deposition process by alternating high shear rates and low shear rates at 60 s intervals. An estimation of the shear rate in the nozzle was first realized using the Rabinowitsch–Mooney equation, according to which a shear rate ($\dot{\Upsilon}$) through a circular orifice of radius (R) for shear-thinning materials can be expressed according to eq 5 (Dealy et Wissbrun 2012).

$$\dot{\gamma} = \frac{4\mathrm{Q}}{\pi\mathrm{R}^3}\left(\frac{3\mathrm{n}+1}{4\mathrm{n}}\right) \qquad eq\ 5$$

Where Q is the volume flow rate and n the flow behavior index of the shear-thinning material. To determine the maximum shear rate which could be reached in our work, we can consider the formulation PFA-Cell28-B (n=0.16) printed using a nozzle with a minimum diameter of 0.5 mm (10 times larger than the largest particle of the powder) with a flow rate of 4.5 mm^3/min (corresponding to a printing speed of 1800 mm/min). In these conditions, the shear rate would be 848 1/s.

Unfortunately, shearing such complex suspensions at this value of rate on the rotational rheometer was not possible because of edge fracture phenomenon. This kind of sample instability is characterized by a deformation of the sample's surface at the free edges between the upper and lower part of the geometry. This rheological characterization limitation is caused by a deformation of the surface and a secondary flow propagating radially as a function of both time and applied deformation which increases measuring errors at high shear rates (Hemingway, Kusumaatmaja, et Fielding 2017; Meyer et Crawford 2018). For a relevant thixotropic characterization, the formulations were sheared at 100 1/s and 0.1 1/s rates.

The results of the thixotropic shear recovery behavior are illustrated in Figure 7-A. All formulations' viscosity decreased significantly at a high shear rate and recovered more or less rapidly at a low shear rate until reaching stabilized values at the end of the shearing interval. When adding from 16 to 22 wt% of cellulose powder one can notice a drop in viscosity of 2 orders of magnitude reaching up to 3 orders of magnitude when adding more than 25 wt% of particles. When shifting to a low shear rate after 60 s of high rate shearing, the viscosity starts to build up again. In the viscosity build-up phase, a difference between the formulations occurs. The formulation containing the least cellulose builds up more quickly than those containing over 19 wt% cellulose, which can be explained by the difficulty of the highly filled structures to build up again after an important decrease in viscosity and breakage of the particles network. This might also be related to an increase in the temperature of the suspension due to particles friction, which decreases the resin viscosity. To quantify the overall recovery of the viscosity, a recovery percentage R(%) is calculated according to eq 6 where η_{in} is the average viscosity during the last 10 s of step 3 and η_{fin} the average of the viscosity during the last 10 s of step 5.

$$\mathrm{R}(\%) = \frac{\eta_{\mathrm{fin}} \cdot 100}{\eta_{\mathrm{in}}} \qquad \textit{eq 6}$$

Figure 7-B shows the recovery percentage of the inks within 60 s after the removal of the high shear rate (100 1/s) as a function of cellulose powder content. The recovery percentage is dependent on the cellulose weight fraction, which is inversely proportional. This tendency might be due to a permanent disruption of the more entangled network. The viscosity recovery is between 65 and 100%, which is an acceptable value, but for an optimized shape fidelity, this value should be maximized for a total recovery of the structure during layer deposit.

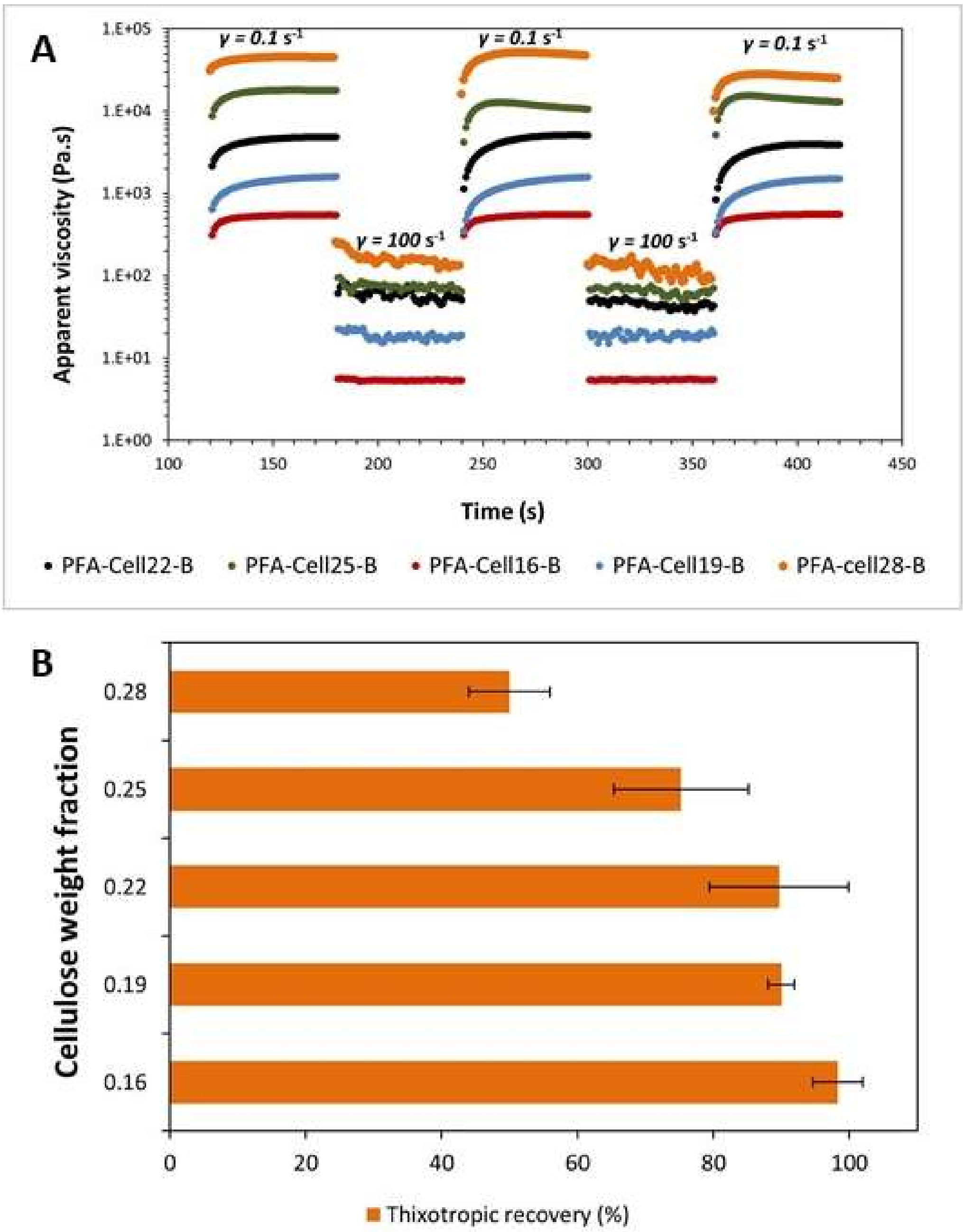

Figure 7 : (A) A 5-step thixotropic behavior study of different suspensions, (B)Thixotropic recovery rate as a function of cellulose weight fraction in different slurries.

3.2 3D printing quality and limitations

Printing with LDM, as highlighted before, can be very restrictive and limiting as for the printable forms, the infill level, the maximum height, and the resolution. Therefore, the printability of the spanning structure with a low infill was inspected using the optimized paste formulation (PFA-Cell28-B). Moreover, the maximum printing height was also evaluated using the current printing process.

Spanning structure and infill

To assess the printability of a spanned structure, we can simply consider the minimum G' required as already suggested in one of the first works dealing with the concept of printability (James E. Smay, Cesarano, et Lewis 2002). The minimum G', given by eq 7, was determined by setting a maximum spanning rod deflection to be 0.05×D, where D is the rod's diameter.

$$\mathrm{G'}_{\mathrm{min}} = 1.4 \cdot \rho \cdot \mathrm{g} \cdot \mathrm{D} \cdot \mathrm{s}^4 \qquad \textit{eq 7}$$

Where ρ is the density of the fresh paste, g is the gravitational constant, and (s=d/D) is the normalized span distance between rods. Therefore, the normalized maximum span distance(s) can be calculated for a known value of G' by rearranging eq 7 (eq 8) with (s=d/D). For printing the paste with a storage modulus of 0.2 MPa, the density of 1.46 g/cm^3, and nozzle diameter of 0.72 mm, the maximum span distance with a deflection inferior to 5% is ~1.45 mm. Nevertheless, it is possible to print span distance up to 10 mm if deflection is accepted until 25%. As one can see in Figure 8-A, the freshly printed filament was only slightly deflected between the edges of the support when reaching a span distance of 10 mm.

$$\mathrm{s}^4 = \frac{\mathrm{G'}}{1.4 \cdot \rho \cdot \mathrm{g}} \qquad \textit{eq 8}$$

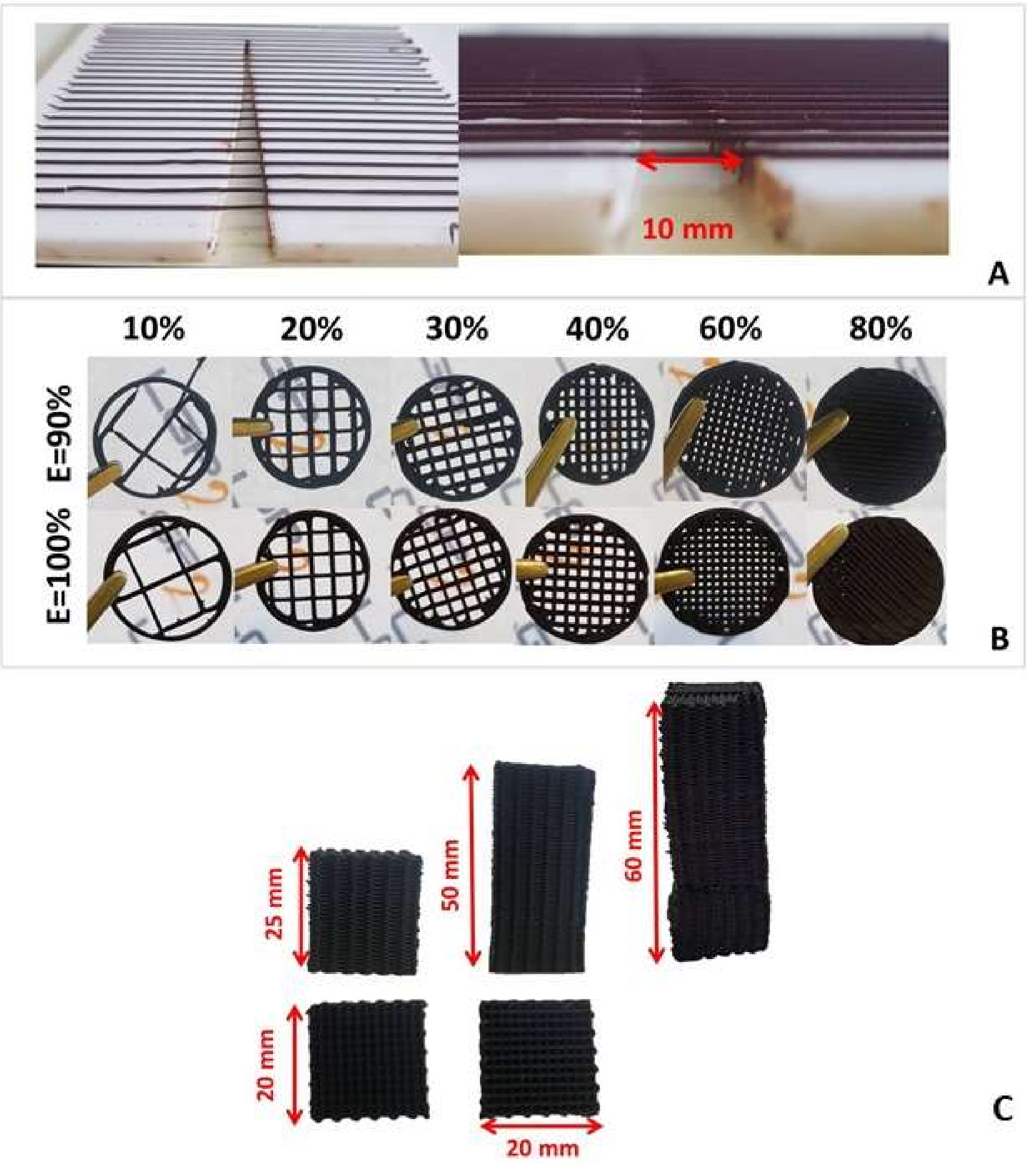

Figure 8: Visual assessment of the spanning structure quality (A) printed filament on plastic support with triangular-shaped hollow part (B) circular spanning structure with different infill percentages and (C) Printed tower of spanned structure with 40% infill with no supporting shell with height ranging from 25 mm to 60 mm.

Furthermore, to assess the performance of the spanned structure, a two-layer circular grid was printed with different infill levels ranging from 10% to 80% which corresponds to a span distance ranging from <0.1 mm to 6 mm. In line with the theoretically calculated span distance, the best-spanned structure with the best quality was obtained when the span distance was inferior to 2 mm which corresponds in our case to 40% rectilinear infill. Moreover, to investigate the effect of the extrusion flow on the quality of the spanned structure, the extrusion flow was decreased by 10% in order to possibly enhance the spanned structure. As one can see in Figure 8-B, this caused either a break of the extruded filament because of the under-extrusion or a very thin deposited filament that does not correspond to the nozzle diameter. Therefore, when printing spanned structure, it is preferred to not exceed a spanning distance with a deflection percentage that does not exceed a maximum of 5% of the nozzle's diameter which can be estimated using eq 8. It is important to highlight that this distance is proper to every printing parameter, and printed paste.

By the same token, the printability of these spanning structures was evaluated on 3D objects by stacking multiple layers and assessing the shape fidelity and the overall stability of the printed part. To do so, towers with a base of 20 mm² and height ranging from 25 mm to 60 mm were printed with 40% infill and with no surrounding contour. As one can notice in Figure 8-C when reaching a height of 25 mm the printed structure was neat and stable with no noticeable defects. When reaching 50 mm the structure was still dimensionally stable and the span structure was also neat as we can see on the top view. But we can notice that the tower is slightly tilted because of the stress exerted on the freshly printed part during the transfer to the oven. When reaching 60 mm, the structure collapsed during the travel as well, nevertheless, the tower was not stable and was continuously moving during the printing because of the force applied by the moving nozzle which created many printing defects.

As explained in the introductory section, the maximum height, which can be supported by the fresh paste without collapsing under its weight, can be estimated using eq 9. The maximum height (H_{max}) is estimated to be around 55 mm when printing with the optimized ink. These results are in agreement with the observations done previously.

When the form factor of the printed part exceeds 2, destabilization can take place because of the printing forces and also the displacement at the end of the printing process. When curing ex-situ, is preferred to not exceed a form factor of 2 and to let the object dry in the open air at room temperature to increase its stiffness before displacing it.

$$\mathrm{H}_{\mathrm{max}} = \frac{\tau_{\mathrm{y}}}{\rho \cdot \mathrm{g}} \qquad \textit{eq 9}$$

Complex structures and printing limitations

Printing by LDM technique presents different challenges than printing thermoplastics by fused filament fabrication. These challenges are mostly related to the latent solidification when printing thermosets as in our case. Indeed, deposing an Nth layer on top of a soggy N-1 layer can cause many issues and limits the possible printing forms and features. For instance, bridging and overhangs can be particularly challenging with the current rheological performances of the paste which is commonly reported by other authors when printing thermoset-based inks where we can rarely see any printed complex structures. However, the printability of more complex parts as shown in Figure 9-A was possible and successful such as the ring with a low overhang angle, a thin-walled vase (2 shells) with detailed textures. Nevertheless, several printing defects can be detected. Indeed, a distinct mark of z-seam when the nozzle starts a new layer can be observed in Figure 9-A. This defect is not particular to the printed paste and is a classic issue that can be faced when printing thermoplastics as well, but this issue can be widened when the sticky filament sticks to the nozzle tip when changing positions, especially at higher acceleration values. This same phenomenon affected also the quality of corners when printing rectangular objects where the corner gets round which is a common challenge when printing with the DIW technique (Feilden 2017; Thibaut et al. 2019). Furthermore, the air bubbles embedded during the mixing and the loading in the cartridge caused the filament (road) to break as one can notice in Figure 9-A.

Moreover, to assess the shape fidelity, cured printed objects were scanned to compare their dimensions to those of the digital design simulation generated by the slicer. As shown in Figure 9-B, the scan of a cube with 40% infill and without any supporting shell showed less than 7% height inaccuracy compared to the slicer simulation which is due to the combined effect of the post-curing shrinkage of the thermosetting resin and the slight effect of the weight of the layers. On the other hand, the first layer of the cube has a side 3.7% smaller than the designed model which is most likely due to the post-curing shrinkage of the resin. However, the top layer is 12.4% smaller than the designed dimension which is believed to be due to both the free shrinkage of the thermosetting resin and especially the printing forces applied on the unsupported cube edges which caused the ‘drugging’ of the filament and hence reduction of the layer’s dimensions. Furthermore, the scan of a well-supported printed ring with 100% infill and shell outlines, given in Figure 9-C, showed an approximately 3% shrinkage compared to the simulated dimensions of the inner diameter, the outer diameter, and the height (respectively 2.92%, 3.20%, and 3.03%) which is believed to be due to the overall shrinkage of the thermosetting resin.

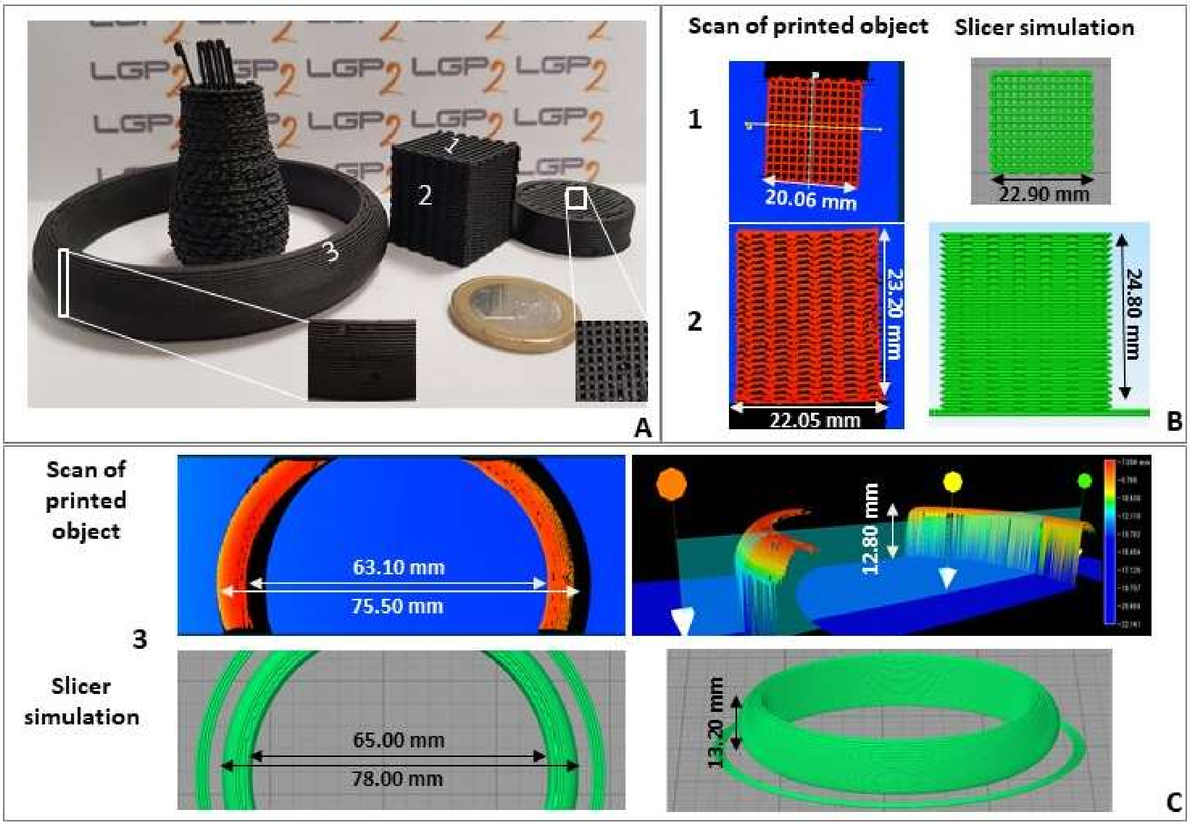

Figure 9: A selection of printed objects with a zoom on the possible defects (A), real scans, and simulation of a top view and lateral view of an unsupported printed cube (B) and a top view and 3D view of a filled printed ring (C).

3.3 Effect of 3D printing parameters on mechanical performances

The influence of the main extrusion settings on the mechanical performances and the morphology of the fractured sample was assessed. To do so, different flexural bars were printed by varying the layer height, and the raster angle while keeping the rest of the parameters fixed such as the nozzle size and the printing speed. The layer height, ranged from 0.36 to 0.65 mm, meaning that the layer height values vary from 50% to 90% of the nozzle diameter (H%). The raster angle was varied between 0° and 90° compared to the x axis of the printer.

Layer height effect

In the literature, the effect of layer height is not clearly understood and contradictory results can be found on whether the layer height has an effect on mechanical performances and which proportionality is there between these values. Many studies were conducted with different printing techniques and parameters and some authors found that an increase in layer height increases the mechanical properties and some others found the contrary. Moreover, it was stated that the layer height can have a different effect on flexural and tensile performances (Vaezi et Chua 2011) and might change by changing the printing parameters such as raster angle, the building orientation, or even the flow rate (Chacón et al. 2017). These different results are caused by the absence of a common methodology to assess printed parts strength when modifying printing parameters (Kuznetsov, Tavitov, et Urzhumtcev 2019).

In the case of our study, as one can notice in Figure 10-A/B, the variation of the ultimate bending strength and flexural modulus in the range of layer thickness H% = {50, 65, 80, 90} % were negligible. Nevertheless, one can notice a slight increase in the flexural performance when decreasing the layer height which might be due to a better binding of layers due to filament squeezing. This slight increase of the flexural strength can also be due to a more oval filament (less circular) as we can see in the SEM images in Figure 10-C which limits the 'triangular' inter filament porosity. The difference in the porosity cannot be quantified because of a high intrinsic porosity generated by the water evaporation during the curing process and the presence of air bubbles embedded in the fresh paste. The layer height is directly related to the number of printed layers for a given object and hence to the printing time which should be minimized. Therefore, from a mechanical point of view, the effect of layer height can be neglected and a larger layer can be preferred for the printing of this material. Moreover, when decreasing the printing layer height the squeezing of the layer against each other can increase the printing force on the already-printed fresh object which might cause the deformation of the object especially when printing objects with a high form factor. However, one should keep in mind that a decrease in layer height is recommended to print objects with overhangs in order to increase the section of the filament supported by the previous layer (Thibaut et al. 2019).

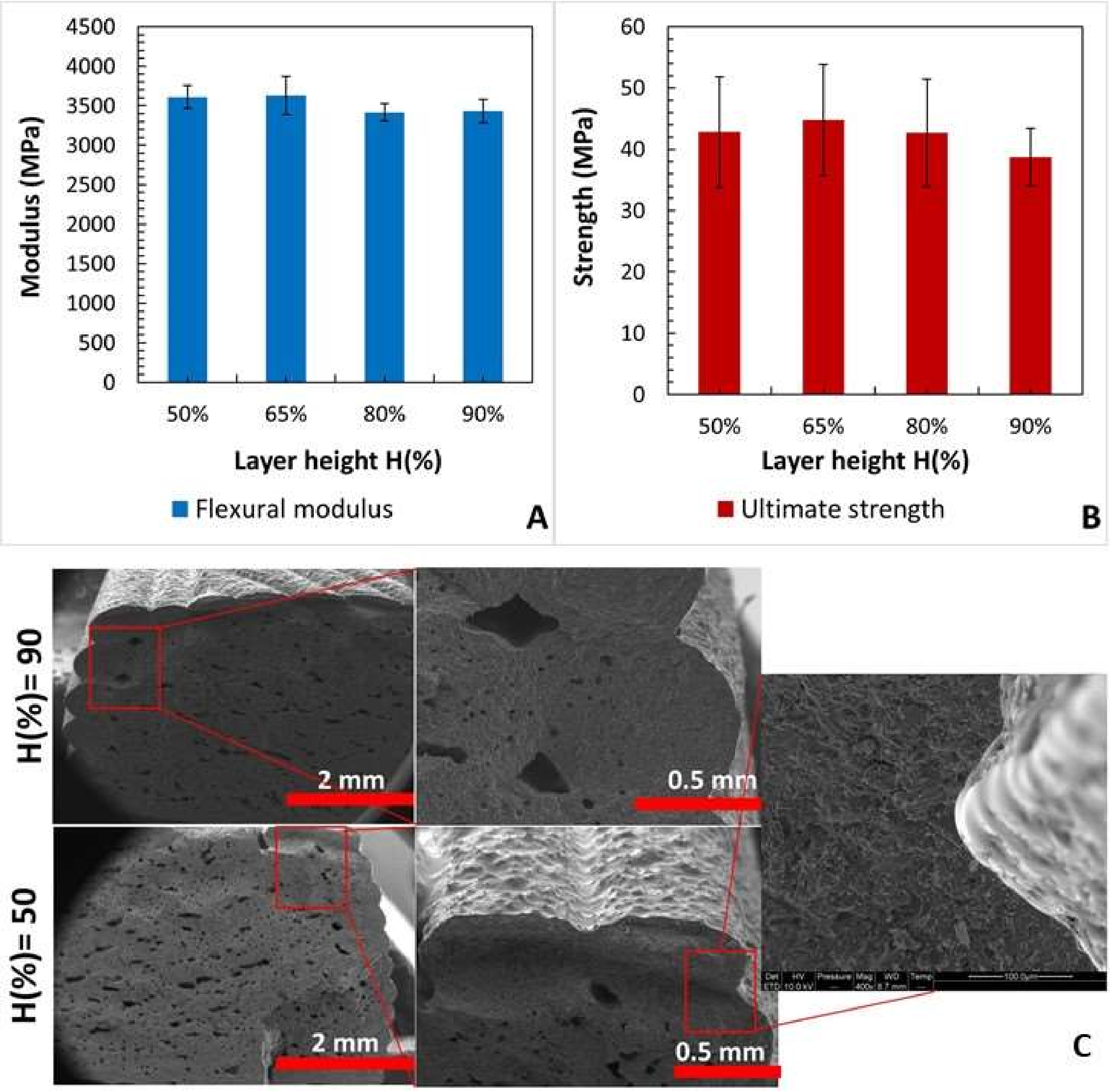

Figure 10: Effect of layer height on the mechanical performances of printed bars. (A) Evolution of flexural modulus as a function of layer height. (B) Evolution of the ultimate flexural strength as a function of the layer height and (C) SEM images of a fracture surface of bending specimens with a layer height of 0.65 mm (top) and 0.36 mm (below) printed with a road width of 0.72 mm and 100% extrusion flow and with 45° infill raster angle.

Raster angle effect

Raster angle is one of the most important parameters of 3D printing which makes the printed object highly anisotropic. Most of the work in the literature agreed that a raster angle of 90° (in the load direction) provided the best mechanical performance as the printed filaments are in the direction of the load. Moreover, when printing composites with high-aspect-ratio fillers, the anisotropy of the material is even magnified. To assess the anisotropy of the printed composites in the present work, the flexural performances of bars printed with a raster angle of 90° and 0° are compared.

It is worth highlighting that in bars printed with a raster angle of 0°, the load is perpendicular to the oriented filaments and parallel to the inter-filamentary interface. As one can observe in Figure 11-A, the flexural modulus along the printing direction is slightly higher than the modulus measured on samples with raster printed at 0°, which can probably be due to the effect of the shear-induced cellulose particles or to an imperfect inter-filamentary adhesion in the bars printed at angles 0°. However, in terms of flexural ultimate strength (Figure 11-B), no significate difference can be detected between the bars printed in both directions except for a higher dispersion in the values of the strength obtained when the load is in along the printing direction. The ultimate strength in the printing direction could reach 50 MPa with an average of 41 MPa.

On SEM images of the fractured cross-section in Figure 11-C, no significant difference can be detected between the two specimens except for a slightly more important pore size which seems to be propagated across the surface which might be a sign of a poor layer adhesion in the core of the specimen. However, when zooming on the edge of both specimens, the inter-layer adhesion seems to be adequate with no signs of delamination. The water evaporation during curing is therefore the main responsible for the cracks embedded between the layers which might be the reason behind the slight decrease in stiffness.

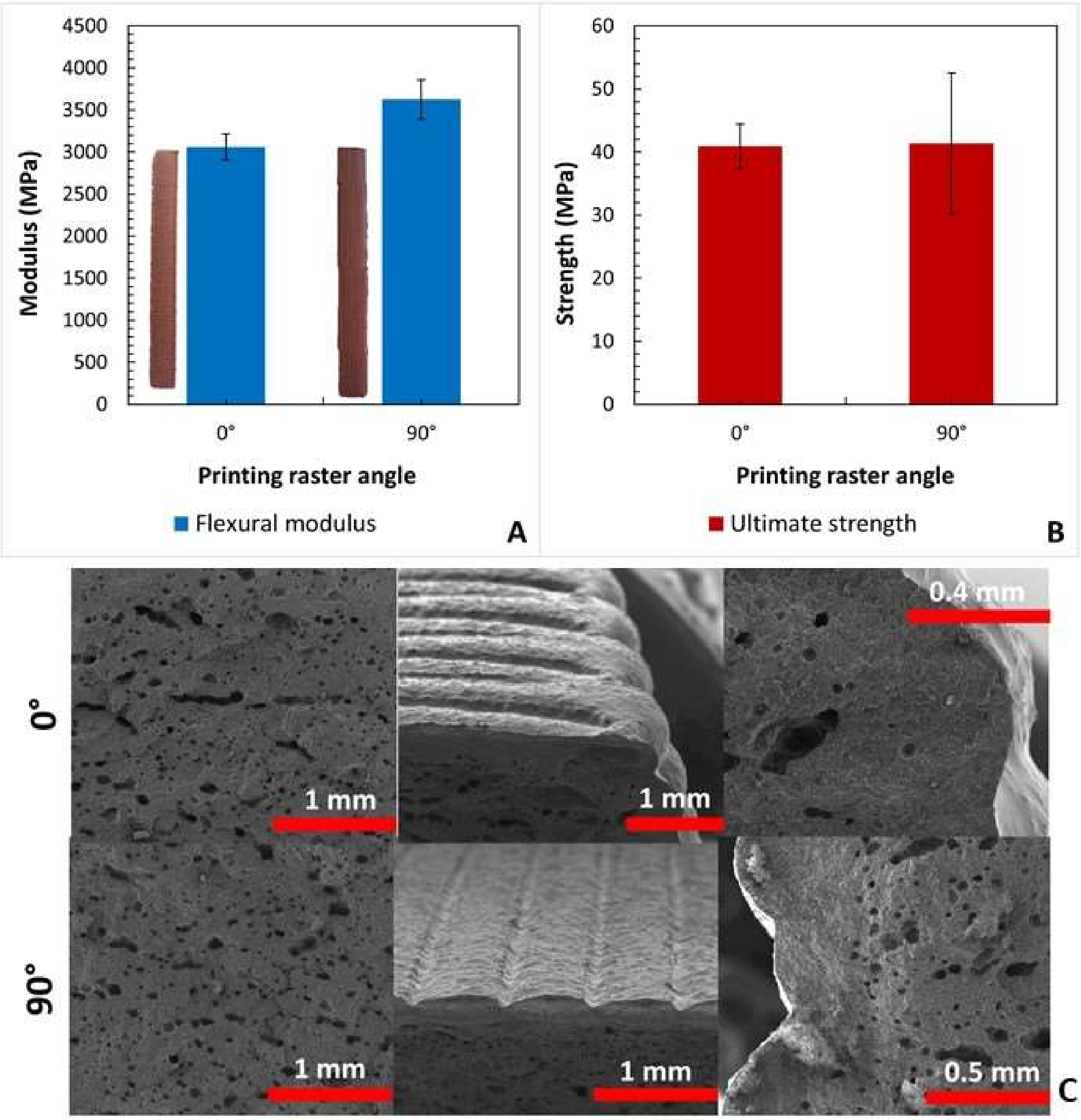

Figure 11: Effect of raster angle on the flexural modulus (A) and the ultimate strength (B), and (C) SEM images of a fracture surface of bending specimens with a raster angle of 0° (top) and 90° (bottom).

The equality in the strength of both types of specimens suggests also that there is no effect of particles alignment along the raster direction. Usually, the alignment of the particles is proportional to the shear rate ($\dot{\gamma}$) applied on the extrudate which also depends on the nozzle size (R) and type, and the extrusion rate as suggested by Rabinowitsch–Mooney in equation (eq 10) where Q is the volume flow rate and n is the thinning exponent of the shear-thinning material. A filament was extruded using a large nozzle of 1 mm and a more restrictive nozzle with 0.5 mm diameter with a low and high extrusion rotation speed of respectively 25 and 275 rpm (which is directly correlated with extrusion flow rate).

$$\dot{\gamma} = \frac{4Q}{\pi R^3}\left(\frac{3n+1}{4n}\right) \qquad \textit{eq 10}$$

When extruding with the large nozzle, Figure 12-A shows the presence of pores in the core of the filament, whereas nearly no pores are observed in the first 150-200 µm below the filament surface. This pores distribution was associated with an effective vapor degassing close to the filament surface and vapor segregation in the filament core. Particles seem to be randomly oriented with no clear orientation in the extrusion direction as we can see on the surface of the filament in the zoomed image on the cross-section where one can notice that some of the cellulose fibers are parallel to the surface of the fractured region and some of them are even broken transversally which can explain the isotropy of the resulting material. No difference was noticed when increasing the extrusion flow rate except for a slight decrease in the porosity but this difference is marginal.

Whilst for the filament extruded with a 0.5 mm nozzle, the first change one can notice is the decrease in the porosity of the filament, which is due to the decrease in the thickness of the filament which facilitates the water evaporation and degassing during the curing phase. In terms of particles alignment, no effect could be noticed as one can see in Figure 12-B, when further increasing the shear rate, the surface of the filament displays the same roughness with no visible alignment, as confirmed by the zoomed observation on the cross-section. This non-alignment of cellulose particles is not surprising as the aspect ratio of the used particle is limited. However, in the case of the addition of a larger fraction of longer fiber, the anisotropy of the printed object should be taken into consideration.

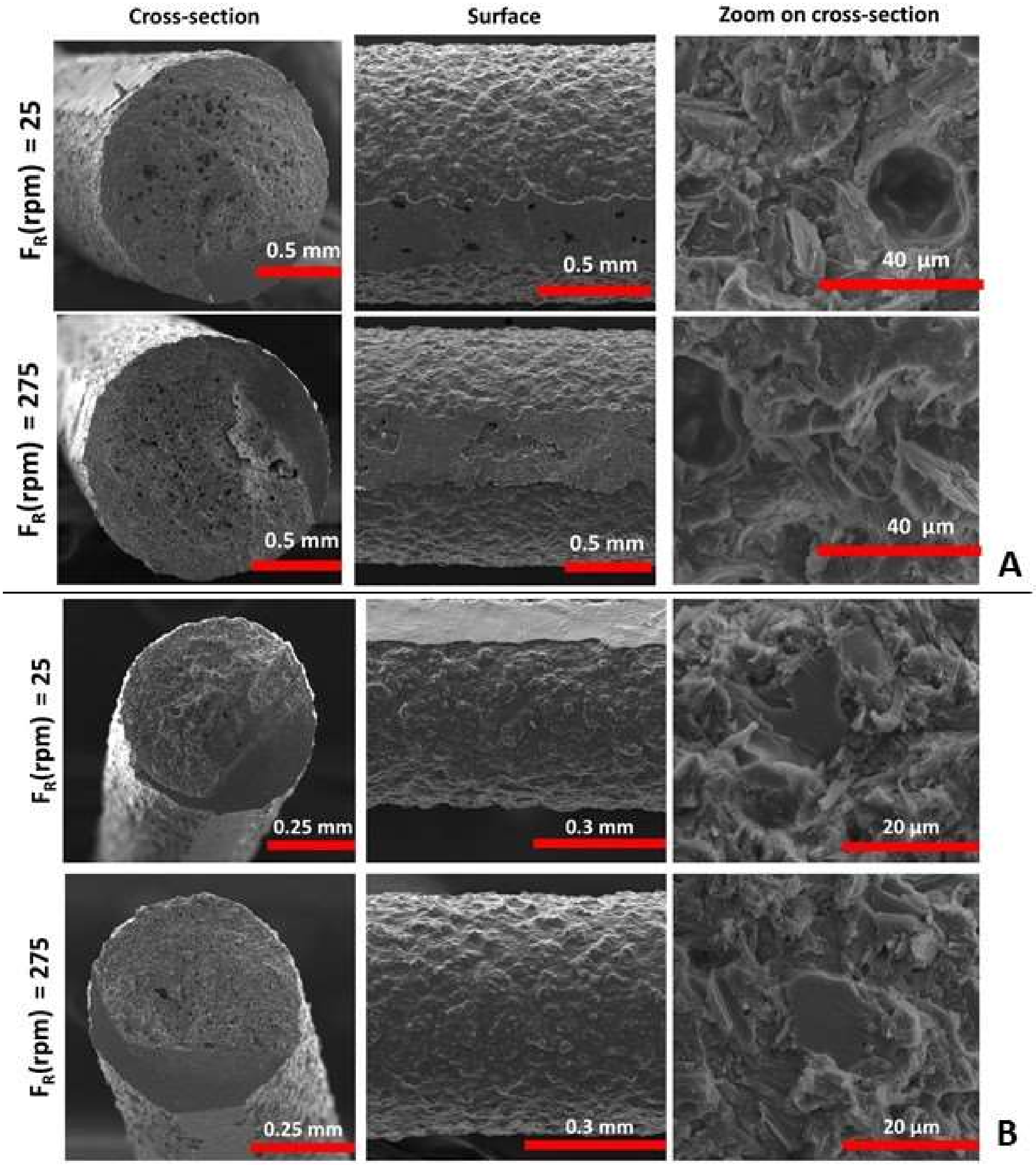

Figure 12: SEM images of an extruded filament through (A) 1 mm nozzle and (B) 0.5 mm nozzle with two different levels of extrusion flow rate.

4 Conclusions

In this work, a new fully bio-based composite material for 3D printing by extrusion was developed. The material formulation was optimized based on the use of a bio-based poly(furfuryl alcohol) thermosetting resin which played the role of a binder and cellulose powder which was used as a rheology modifier to tune the rheological properties of the slurry. To optimize the printability of the slurry, 6 different formulations were prepared with varied cellulose content and the rheological behavior was characterized to assess their eventual printability. The rheological study revealed that:

- The shear-thinning behavior of all the slurries is maximized with the addition of at least 25 wt% fillers.
- The yield stress and stiffness increased with the increase of fillers content, to reach respectively 1.46 kPa and 270 kPa when adding 29 wt% of cellulose powder.
- The slurries containing cellulose powder exhibited a thixotropic behavior, but the viscosity recovery decreased when increasing the cellulose content and it was limited to 60% when adding 28 wt% of fillers, against 98% when adding only 16% of cellulosic particles.

According to these rheology features, the ink formulation containing at least 25 wt% of cellulose and less than 6.6 wt% of solvent (imported by the resin and the catalyst) has the highest potential for 3D printing by material extrusion.

Furthermore, the effect of layer height, and raster angle, on mechanical performances were addressed. It was found that these parameters have no significant effect on the mechanical properties of the tested specimens. However, it is recommended to limit the layer thickness. On the other hand, the inter-layer and inter-filamentary adhesion were shown to be optimum which discarded the delamination issues. In general, the printed specimens exhibited a flexural modulus ranging from 3 to 3.5 GPa and ultimate strength between 40 and 50 MPa.

Finally, the printing quality of the developed material was demonstrated to be adequate for the fabrication of simple and relatively more complex objects.

Acknowledgments

This work was supported by the Région Rhône-Alpes with Pack Ambition Recherche 3DPapEl 2017-2021 grant and Labcom IDEX Thermobiocomp3D 2019-2022 grant. The LGP2 laboratory is part of the LabEx Tec 21 (Investissements d’Avenir: grant agreement no. ANR-11-LABX-0030) and the PolyNat

Carnot Institute (Investissements d’Avenir: grant agreement no. ANR-16-CARN-0025-01). This research was possible owing to the facilities of the TekLiCell platform funded by the Région Rhône-Alpes (ERDF: European Regional Development Fund).

References

Abouzeid, Ragab E., Ramzi Khiari, Davide Beneventi, et Alain Dufresne. 2018. « Biomimetic Mineralization of Three-Dimensional Printed Alginate/TEMPO-Oxidized Cellulose Nanofibril Scaffolds for Bone Tissue Engineering ». *Biomacromolecules* 19(11):4442-52. doi: 10.1021/acs.biomac.8b01325.

Beach, James, Steven Patterson, Alisa Zlatanic, Jamie M. Messman, et Petar R. Dvornic. 2021. « New “All-in-One” Silicone Pastes for Additive Manufacturing of Elastomer Parts ». *MRS Communications* 11(2):88-93. doi: 10.1557/s43579-020-00007-7.

Berretta, S., R. Davies, Y. T. Shyng, Y. Wang, et O. Ghita. 2017. « Fused Deposition Modelling of High Temperature Polymers: Exploring CNT PEEK Composites ». *Polymer Testing* 63:251-62. doi: 10.1016/j.polymertesting.2017.08.024.

Chacón, J. M., M. A. Caminero, E. García-Plaza, et P. J. Núñez. 2017. « Additive Manufacturing of PLA Structures Using Fused Deposition Modelling: Effect of Process Parameters on Mechanical Properties and Their Optimal Selection ». *Materials & Design* 124:143-57. doi: 10.1016/j.matdes.2017.03.065.

Chu, S. H., L. G. Li, et A. K. H. Kwan. 2021. « Development of Extrudable High Strength Fiber Reinforced Concrete Incorporating Nano Calcium Carbonate ». *Additive Manufacturing* 37:101617. doi: 10.1016/j.addma.2020.101617.

Compton, Brett. 2015. « 3D Printing of Composites with Controlled Architecture ». 30.

Compton, Brett G., Nadim S. Hmeidat, Robert C. Pack, Maximilian F. Heres, et Joshua R. Sangoro. 2018. « Electrical and Mechanical Properties of 3D-Printed Graphene-Reinforced Epoxy ». *JOM* 70(3):292-97. doi: 10.1007/s11837-017-2707-x.

Dealy, John M., et K. F. Wissbrun. 2012. *Melt Rheology and Its Role in Plastics Processing: Theory and Applications*. Springer Science & Business Media.

Duty, Chad, Christine Ajinjeru, Vidya Kishore, Brett Compton, Nadim Hmeidat, Xun Chen, Peng Liu, Ahmed Arabi Hassen, John Lindahl, et Vlastimil Kunc. 2018. « What Makes a Material Printable? A Viscoelastic Model for Extrusion-Based 3D Printing of Polymers ». *Journal of Manufacturing Processes* 35:526-37. doi: 10.1016/j.jmapro.2018.08.008.

Fahmy, Ahmed Raouf, Thomas Becker, et Mario Jekle. 2020. « 3D Printing and Additive Manufacturing of Cereal-Based Materials: Quality Analysis of Starch-Based Systems Using a Camera-Based Morphological Approach ». *Innovative Food Science & Emerging Technologies* 63:102384. doi: 10.1016/j.ifset.2020.102384.

Feilden, Ezra. 2017. « Additive Manufacturing of Ceramics and Ceramic Composites via Robocasting ». doi: 10.25560/55940.

Feilden, Ezra, Esther García-Tuñón Blanca, Finn Giuliani, Eduardo Saiz, et Luc Vandeperre. 2016. « Robocasting of Structural Ceramic Parts with Hydrogel Inks ». *Journal of the European Ceramic Society* 36(10):2525-33. doi: 10.1016/j.jeurceramsoc.2016.03.001.

Gillispie, Gregory, Peter Prim, Joshua Copus, John Fisher, Antonios G. Mikos, James J. Yoo, Anthony Atala, et Sang Jin Lee. 2020. « Assessment Methodologies for Extrusion-Based Bioink Printability ». *Biofabrication* 12(2):022003. doi: 10.1088/1758-5090/ab6f0d.

Håkansson, Karl M. O., Ida C. Henriksson, Cristina de la Peña Vázquez, Volodymyr Kuzmenko, Kajsa Markstedt, Peter Enoksson, et Paul Gatenholm. 2016. « Solidification of 3D Printed Nanofibril Hydrogels into Functional 3D Cellulose Structures ». *Advanced Materials Technologies* 1(7):1600096. doi: https://doi.org/10.1002/admt.201600096.

Han, Xingting, Dong Yang, Chuncheng Yang, Sebastian Spintzyk, Lutz Scheideler, Ping Li, Dichen Li, Jürgen Geis-Gerstorfer, et Frank Rupp. 2019. « Carbon Fiber Reinforced PEEK Composites Based on 3D-Printing Technology for Orthopedic and Dental Applications ». *Journal of Clinical Medicine* 8(2):240. doi: 10.3390/jcm8020240.

Hemingway, Ewan, Halim Kusumaatmaja, et Suzanne Fielding. 2017. « Edge Fracture in Complex Fluids ». *Physical Review Letters* 119. doi: 10.1103/PhysRevLett.119.028006.

Hmeidat, Nadim S., James W. Kemp, et Brett G. Compton. 2018. « High-Strength Epoxy Nanocomposites for 3D Printing ». *Composites Science and Technology* 160:9-20. doi: 10.1016/j.compscitech.2018.03.008.

Hmeidat, Nadim S., Robert C. Pack, Samantha J. Talley, Robert B. Moore, et Brett G. Compton. 2020. « Mechanical Anisotropy in Polymer Composites Produced by Material Extrusion Additive Manufacturing ». *Additive Manufacturing* 34:101385. doi: 10.1016/j.addma.2020.101385.

Hong, Jingmin, Jing Zhou, et Jinglan Hong. 2015. « Environmental and Economic Impact of Furfuralcohol Production Using Corncob as a Raw Material ». *The International Journal of Life Cycle Assessment* 20(5):623-31. doi: 10.1007/s11367-015-0854-2.

Jiang, Jungang, Hale Oguzlu, et Feng Jiang. 2021. « 3D Printing of Lightweight, Super-Strong yet Flexible All-Cellulose Structure ». *Chemical Engineering Journal* 405:126668. doi: 10.1016/j.cej.2020.126668.

Klar, Ville, Jaakko Pere, Tuomas Turpeinen, Pyry Kärki, Hannes Orelma, et Petri Kuosmanen. 2019. « Shape Fidelity and Structure of 3D Printed High Consistency Nanocellulose ». *Scientific Reports* 9(1):3822. doi: 10.1038/s41598-019-40469-x.

Krajangsawasdi, Narongkorn, Lourens G. Blok, Ian Hamerton, Marco L. Longana, Benjamin K. S. Woods, et Dmitry S. Ivanov. 2021. « Fused Deposition Modelling of Fibre Reinforced Polymer Composites: A Parametric Review ». *Journal of Composites Science* 5(1):29. doi: 10.3390/jcs5010029.

Kraut, Gabriele, Laura Yenchesky, Fermin Prieto, Günter E. M. Tovar, et Alexander Southan. 2017. « Influence of Shear Thinning and Material Flow on Robotic Dispensing of Poly(Ethylene Glycol) Diacrylate/Poloxamer 407 Hydrogels ». *Journal of Applied Polymer Science* 134(29):45083. doi: 10.1002/app.45083.

Kuznetsov, Vladimir E., Azamat G. Tavitov, et Oleg D. Urzhumtcev. 2019. « Hardware Factors Influencing Interlayer Bonding Strength of Parts Obtained by Fused Filament Fabrication ». doi: 10.20944/preprints201905.0108.v1.

La Rosa, Angela, Giulia Cozzo, Alberta Latteri, Giuseppe Mancini, Antonino Recca, et Gianluca Cicala. 2013. « A Comparative Life Cycle Assessment of a Composite Component for Automotive ». *Chemical Engineering Transaction* 32. doi: 10.3303/CET1332288.

Lei, Dong, Yang Yang, Zenghe Liu, Shuo Chen, Benyan Song, Ao Shen, Binqian Yang, Sen Li, Zhize Yuan, Quan Qi, Lijie Sun, Yifan Guo, Han Zuo, Shixing Huang, Qi Yang, Xiumei Mo, Chuanglong He, Bo Zhu, Eric M. Jeffries, Feng-Ling Qing, Xiaofeng Ye, Qiang Zhao, et Zhengwei You. 2019. « A General Strategy of 3D Printing Thermosets for Diverse Applications ». *Materials Horizons* 6(2):394‑404. doi: 10.1039/C8MH00937F.

Leppiniemi, Jenni, Panu Lahtinen, Antti Paajanen, Riitta Mahlberg, Sini Metsä-Kortelainen, Tatu Pinomaa, Heikki Pajari, Inger Vikholm-Lundin, Pekka Pursula, et Vesa P. Hytönen. 2017. « 3D-Printable Bioactivated Nanocellulose–Alginate Hydrogels ». *ACS Applied Materials & Interfaces* 9(26):21959‑70. doi: 10.1021/acsami.7b02756.

Li, Huijun, Sijun Liu, et Li Lin. 2016. « Rheological Study on 3D Printability of Alginate Hydrogel and Effect of Graphene Oxide ». *International Journal of Bioprinting* 2. doi: 10.18063/IJB.2016.02.007.

Lille, Martina, Asta Nurmela, Emilia Nordlund, Sini Metsä-Kortelainen, et Nesli Sozer. 2018. « Applicability of Protein and Fiber-Rich Food Materials in Extrusion-Based 3D Printing ». *Journal of Food Engineering* 220:20‑27. doi: 10.1016/j.jfoodeng.2017.04.034.

Malek, Sardar, Jordan R. Raney, Jennifer A. Lewis, et Lorna J. Gibson. 2017. « Lightweight 3D Cellular Composites Inspired by Balsa ». *Bioinspiration & Biomimetics* 12(2):026014. doi: 10.1088/1748-3190/aa6028.

Markstedt, Kajsa, Athanasios Mantas, Ivan Tournier, Héctor Martínez Ávila, Daniel Hägg, et Paul Gatenholm. 2015. « 3D Bioprinting Human Chondrocytes with Nanocellulose–Alginate Bioink for Cartilage Tissue Engineering Applications ». *Biomacromolecules* 16(5):1489‑96. doi: 10.1021/acs.biomac.5b00188.

M'Barki, Amin, Lydéric Bocquet, et Adam Stevenson. 2017. « Linking Rheology and Printability for Dense and Strong Ceramics by Direct Ink Writing ». *Scientific Reports* 7(1):6017. doi: 10.1038/s41598-017-06115-0.

Meyer, Fabian, et Nate Crawford. 2018. « Optimizing Process Conditions and Ensuring End Product Requirements of Plastics with Rheological Analysis ». 7.

Montoya, Juliana, Jorge Medina, Arturo Molina, Janet Gutiérrez, Blanca Rodríguez, et Rodrigo Marín. 2021. « Impact of Viscoelastic and Structural Properties from Starch-Mango and Starch-Arabinoxylans Hydrocolloids in 3D Food Printing ». *Additive Manufacturing* 39:101891. doi: 10.1016/j.addma.2021.101891.

Naghieh, Saman, et Daniel Chen. 2021. « Printability – a Key Issue in Extrusion-Based Bioprinting ». *Journal of Pharmaceutical Analysis*. doi: 10.1016/j.jpha.2021.02.001.

Niu, Yongan, Shuojin Zheng, Pingan Song, Xin Zhang, et Chao Wang. 2021. « Mechanical and Thermal Properties of PEEK Composites by Incorporating Inorganic Particles Modified Phosphates ». *Composites Part B: Engineering* 212:108715. doi: 10.1016/j.compositesb.2021.108715.

Panda, Biranchi, Suvash Chandra Paul, Lim Jian Hui, Yi Wei Daniel Tay, et Ming Jen Tan. 2017. « Additive Manufacturing of Geopolymer for Sustainable Built Environment ». *Journal of Cleaner Production* 167:281-88. doi: 10.1016/j.jclepro.2017.08.165.

Panda, Biranchi, Cise Unluer, et Ming Jen Tan. 2018. « Investigation of the Rheology and Strength of Geopolymer Mixtures for Extrusion-Based 3D Printing ». *Cement and Concrete Composites* 94:307-14. doi: 10.1016/j.cemconcomp.2018.10.002.

Panda, Biranchi, Cise Unluer, et Ming Jen Tan. 2019. « Extrusion and Rheology Characterization of Geopolymer Nanocomposites Used in 3D Printing ». *Composites Part B: Engineering* 176:107290. doi: 10.1016/j.compositesb.2019.107290.

Pattinson, Sebastian W., et A. John Hart. 2017. « Additive Manufacturing of Cellulosic Materials with Robust Mechanics and Antimicrobial Functionality ». *Advanced Materials Technologies* 2(4):1600084. doi: https://doi.org/10.1002/admt.201600084.

Rieger, Thomas, Tim Schubert, Julian Schurr, Marcel Butschle, Michael Schwenkel, Timo Bernthaler, et Gerhard Schneider. 2021. « Slurry Development for Lithography-Based Additive Manufacturing of Cemented Carbide Components ». *Powder Technology* 383:498-508. doi: 10.1016/j.powtec.2021.01.049.

Segal, L., J. J. Creely, A. E. Martin, et C. M. Conrad. 1959. « An Empirical Method for Estimating the Degree of Crystallinity of Native Cellulose Using the X-Ray Diffractometer ». *Textile Research Journal* 29(10):786-94. doi: 10.1177/004051755902901003.

Shang, Jianzhong, Xin Li, Rong Wang, et Zhuo Wang. 2017. « Rheological and Printable Behavior of Epoxy Resin-based Materials for Extrusion 3D Printing Applications ». 폴리머 41(5):874-81. doi: 10.7317/pk.2017.41.5.874.

Shi, Qian, Kai Yu, Xiao Kuang, Xiaoming Mu, Conner K. Dunn, Martin L. Dunn, Tiejun Wang, et H. Jerry Qi. 2017. « Recyclable 3D Printing of Vitrimer Epoxy ». *Materials Horizons* 4(4):598-607. doi: 10.1039/C7MH00043J.

Smay, J. E., G. M. Gratson, R. F. Shepherd, J. Cesarano, et J. A. Lewis. 2002. « Directed Colloidal Assembly of 3D Periodic Structures ». *Advanced Materials* 14(18):1279-83. doi: 10.1002/1521-4095(20020916)14:18<1279::AID-ADMA1279>3.0.CO;2-A.

Smay, James E., Joseph Cesarano, et Jennifer A. Lewis. 2002. « Colloidal Inks for Directed Assembly of 3-D Periodic Structures ». *Langmuir* 18(14):5429-37. doi: 10.1021/la0257135.

Sultan, Sahar, Gilberto Siqueira, Tanja Zimmermann, et Aji P. Mathew. 2017. « 3D Printing of Nano-Cellulosic Biomaterials for Medical Applications ». *Current Opinion in Biomedical Engineering* 2:29-34. doi: 10.1016/j.cobme.2017.06.002.

Thibaut, C., A. Denneulin, S. Rolland du Roscoat, D. Beneventi, L. Orgéas, et D. Chaussy. 2019. « A Fibrous Cellulose Paste Formulation to Manufacture Structural Parts Using 3D Printing by Extrusion ». *Carbohydrate Polymers* 212:119-28. doi: 10.1016/j.carbpol.2019.01.076.

Vaezi, Mohammad, et Chee Kai Chua. 2011. « Effects of Layer Thickness and Binder Saturation Level Parameters on 3D Printing Process ». *The International Journal of Advanced Manufacturing Technology* 53(1-4):275-84. doi: 10.1007/s00170-010-2821-1.

Vinyas, M., Sj Athul, D. Harursampath, et T. Nguyen Thoi. 2019. « Experimental Evaluation of the Mechanical and Thermal Properties of 3D Printed PLA and Its Composites ». *Materials Research Express* 6(11):115301. doi: 10.1088/2053-1591/ab43ab.

Yang, Kejia, Jesse C. Grant, Patrice Lamey, Alexandra Joshi-Imre, Benjamin R. Lund, Ronald A. Smaldone, et Walter Voit. 2017. « Diels–Alder Reversible Thermoset 3D Printing: Isotropic Thermoset Polymers via Fused Filament Fabrication ». *Advanced Functional Materials* 27(24):1700318. doi: https://doi.org/10.1002/adfm.201700318.

Zhang, Yu, Yunsheng Zhang, Wei She, Lin Yang, Guojian Liu, et Yonggan Yang. 2019. « Rheological and Harden Properties of the High-Thixotropy 3D Printing Concrete ». *Construction and Building Materials* 201:278-85. doi: 10.1016/j.conbuildmat.2018.12.061.